Progress In Electromagnetics Research B, Vol. 95, 61–79, 2022

Miniaturized Dual-Band Embedded NZI Metasurface Antenna with Front-to-Back Radiation Ratio Enhancement

Parul Dawar[1, *] and Mahmoud A. Abdalla[2]

Abstract—In this paper, a novel miniaturized dual-band embedded near-zero index (NZI) metasurface-based patch antenna is presented. A new methodology based on loading a narrowband microstrip patch antenna (resonating at 4.6 GHz) by a metasurface embedded in the middle of the antenna's substrate is introduced. The loaded antenna has a dual-band resonance of bandwidths of 15% and 43% at 2 GHz and 4.6 GHz, respectively. The metasurface layer is an array of square holes such that there is no hole below the patch. The metasurface layer is designed as a near-zero-refractive-index material (NZRIM). By controlling the phase reflection properties of the structure, the antenna gain is increased by 5.5 dB, original bandwidth increased ten times and the front-to-back ratio improved from 7 to 187. Also, footprint miniaturization of 56.5% with a maximum size of $(1.9\lambda_0)^2$ is obtained. To the best of the authors' knowledge, such enhancement is the largest to date.

1. INTRODUCTION

The continuous need for high directive and low-profile antennas at microwave frequencies is essential for modern applications of satellites, radars, and wireless communication systems. Large aperture array antennas can solve this point, but they are bulky and may need complex feeding networks. Printed microstrip antennas are preferred at microwave frequencies as they are low profile, easily fabricated, and can provide multi-functions in terms of operating frequencies and emitted wave polarization and beam scanning functionality. However, these antennas have some serious limitations like the half-wavelength length of a microstrip patch or microstrip slot antenna, which is large for some portable wireless applications. Also, these antennas' directivity is in the order 6 dB which is also a small value. In addition, microstrip patch antennas have narrow bandwidth typically 1–2% because of the resonant structure.

Different methods have been used to miniaturize the size of microstrip antennas, for example employing high electric permittivity substrates [1–3], using shorting pins/shorting walls [2, 4], using resistive or reactive loading to the patch [5, 6], increasing the electrical length by meandering patch, using slots, and folding the patch [1, 7, 8]. Moreover, composite right/left-handed (CRLH) metamaterial structures [9] and loading antennas with distributed capacitors and/or inductors [10] have also been applied to reduce the size of patch antennas. The size reduction degrades the radiation performance of the antenna in terms of impedance bandwidth ($S_{11} < -10$ dB), gain, and radiation efficiency. A comparison between the radiation performance and size of the conventional patch and L-C loaded compact patch [11] confirmed that a 90% miniaturization of the antenna reduced the gain by 4 dB, bandwidth by 1.6%, and radiation efficiency by 8%. Several other techniques have been used to enhance the impedance bandwidth of the microstrip patch antennas. For example, using thicker and/or lower permittivity substrate [12], multiple resonators in coplanar [13] and stacked configuration [10], new

Received 4 February 2022, Accepted 29 March 2022, Scheduled 21 April 2022

* Corresponding author: Mahmoud Abdelrahman Abdalla (maaabdalla@ieee.org).

[1] Electronics and Communication Engineering Department, Guru Tegh Bahadur Institute of Technology, Delhi, India.

[2] Electromagnetic Waves Group, Department of Electronic Engineering, Military Technical College, Cairo, Egypt.

feeding techniques or impedance matching networks [14], and cutting slots on the patch [15] were used to increase the bandwidth.

The problem of back lobe radiation and surface waves in printed microstrip antennas resulted in reducing the antenna radiation efficiency and could be solved by backing the antennas with conductor reflectors or artificial magnetic conductors [16, 17]. Also, to increase antenna directivity, one successful approach is using Resonant Cavity Antenna (RCA) [18]. RCA is a planar feed antenna loaded with partially reflecting artificial surfaces (PRSs) as superstrates which are usually designed using metasurface.

The metasurface is a two-dimensional surface version of metamaterials that is obtained by arranging electrically small scatters/holes at a surface. Based on the pattern periodicity, the average tangential fields can be controlled using a local Floquet-wave expansion, hence controlling the electromagnetic behavior at the surface [19]. Thanks to the unique electromagnetic manipulation of metasurface structures, metasurface-based antennas are characterized with higher directivity, broader bandwidth, and smaller size than conventional planar antennas [20]. Thus, they have been applied in applications like imaging at microwave frequencies [21, 22]. Moreover, metasurface structures have been further employed in developing Fabry Perot Cavity antennas with small RCS, high directive radiation properties [23–28].

In this paper, a new design is proposed by loading a conventional patch antenna, as a primary radiator, with a new metasurface embedded in its substrate. The novelty of the structure lies in the choice of periodicity of the metasurface which is aperiodic and is used to achieve a wide-band antenna with a high front-to-back lobe ratio and directivity and also in choosing its position which is in the middle of the antenna's substrate. This layer does not cause any impedance matching problems which is a common drawback of the reflective surface implementation with MNZ/ENZ, and hence it improves the impedance bandwidth of the designed antenna structure. Thus, the antenna's contribution of the simultaneous bandwidth and directivity enhancement over conventional microstrip patch antenna is considered state-of-the-art by using just a single layer of reflective surface inside the substrate and has a compact size and lower height than the reported antennas in literature [20–24, 29–32]. Analysis through simulation elucidates that the embedded metasurface composed of an aperiodic array of holes enhances the antenna's performance parameters and downscales the operating frequency leading to miniaturization.

2. ANTENNA GEOMETRY WITH APERIODIC HOLES AS EMBEDDED METASURFACE

2.1. Metasurface Loaded Patch Antenna Design

The geometry of the proposed metasurface antenna is shown in Fig. 1. A hole metasurface layer is embedded in the middle of the dielectric substrate. The holes have slots with width $a = 3\,\text{mm}$ and length $b = 3\,\text{mm}$ and spaced by $D_x \times D_x = 7\,\text{mm}^2$. The metasurface layer width and length are equal and less than the overall antenna ground length by 4 mm on each side. The feeding transmission line was optimized to match a $50\,\Omega$ feeding port.

In the EM simulations whose setup is shown in Fig. 2, with the incident time-varying electromagnetic wave (EM) on the randomly positioned design structure (array of aperiodic holes), an electric boundary is allocated along with the vertical axis (y), magnetic boundary along with longitudinal axis (x) (just like Floquet Boundary conditions), and an open boundary along with the horizontal axis (z) in such a way that the propagating vector is aligned with the open boundary.

The next step is to analyze the function of the proposed metasurface unit cell, and its equivalent circuit model is emphasized. In [33], Marcuvitz elaborated on the Equivalent Circuit technique for a Single Square Loop Frequency Selective Surface to extract its associated lumped circuit parameters (R, L, and C) [34, 35]. Hence, one raw linear array of the proposed square hole (in Fig. 1) is plotted in Fig. 3. The unit cell is an assumed square hole with width = a. The periodicity $D_x = r$.

If a uniform plane wave is polarized in the direction perpendicular to the unit cell, the equivalent circuit parameters can be derived as explained in [36] as follows

$$\frac{\omega_r L}{Z_o} = \frac{a}{r}\cos\theta \times C_1(r, width, \lambda, \theta) \tag{1}$$

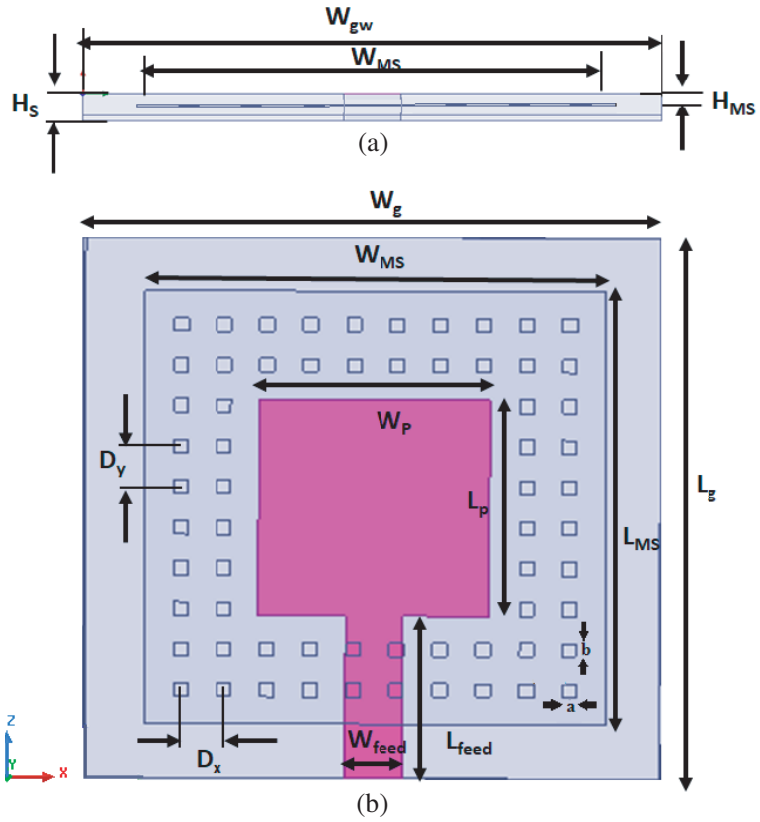

Figure 1. The metasurface antenna geometry ($L_P = W_P = 16\,\text{mm}$, $W_{feed} = 13.92\,\text{mm}$, $L_{feed} = 41.74\,\text{mm}$, $L_{MS} = W_{MS} = 131\,\text{mm}$, $L_g = W_g = 139\,\text{mm}$, $D_X = D_y = 7\,\text{mm}$, $D_{hole} = 3.5\,\text{mm}$). (a) Side View. (b) Top view.

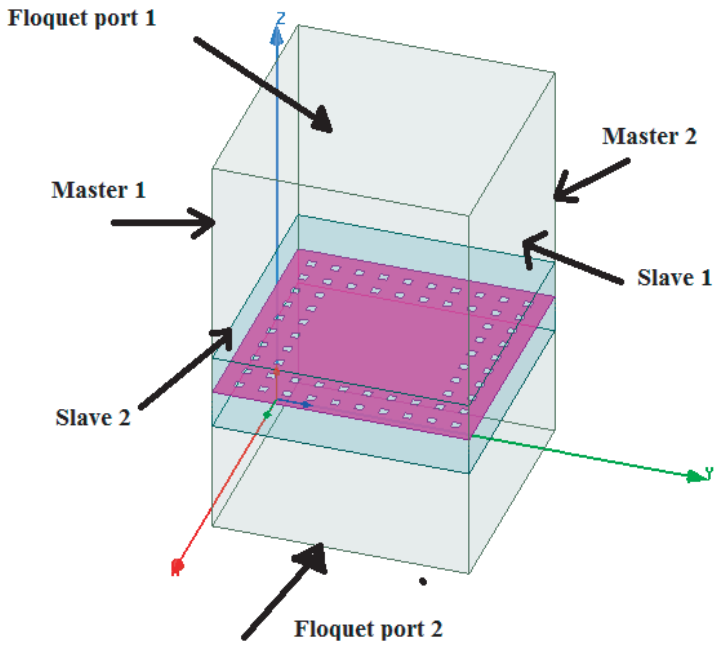

Figure 2. Floquet port analysis configuration for the metasurface PRS layer.

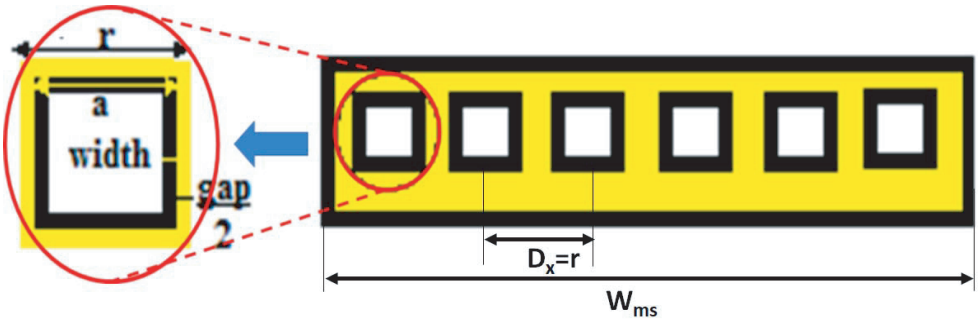

Figure 3. The detailed geometry of array along with its unit cell (white color represents 'no copper' and yellow and black colors are for specifying clarity in visualization and denote 'copper').

where

$$C_1(r, width, \lambda, \theta) = \frac{r}{\lambda}\left[\ln\csc\left(\frac{\pi \cdot width}{2r}\right)\right] + C_2(r, width, \lambda, \theta) \tag{2}$$

$$\frac{\omega_r C}{Y_o} = 4\frac{a}{\lambda}\sec\theta \times C_1(r, gap, \lambda, \theta) \times \varepsilon_{eff} \tag{3}$$

$$C_1(r, gap, \lambda, \theta) = \frac{r}{\lambda}\left[\ln\csc\left(\frac{\pi gap}{2r}\right)\right] + C_2(r, gap, \lambda, \theta) \tag{4}$$

where Z_o, Y_o, ε_{eff}, θ, $C_2(r, width, \lambda, \theta)$, and $C_2(r, gap, \lambda, \theta)$ are the characteristic impedance in free-space, characteristic admittance in free-space, the effective dielectric permittivity of the medium, incident angle, and the systemic errors for inductance and capacitance, respectively. Therefore, Equations (1) and (3) can be written as in Eqs. (5) and (6), respectively.

$$\frac{\omega_r L}{Z_o} = \frac{a}{r}\cos\theta \cdot \frac{r}{\lambda}\ln\csc\left(\frac{\pi \cdot width}{2r}\right) \tag{5}$$

$$\frac{\omega_r C}{Y_o} = \frac{a}{r}\sec\theta \cdot \frac{r}{\lambda}\ln\csc\left(\frac{\pi \cdot gap}{2r}\right) \times \varepsilon_{eff} \tag{6}$$

Assuming dielectric to be air and multiplying Eqs. (5) and (6), then,

$$\omega_r^2 LC = 4\left(\frac{a}{r}\right)^2\left(\frac{r}{\lambda}\right)^2 \times \ln\csc\left(\frac{\pi \cdot width}{2r}\right)\ln\csc\left(\frac{\pi \cdot gap}{2r}\right) \tag{7}$$

The LHS of Eq. (7) shows resonant or anti-resonant phenomenon. Considering this PRS as ideally reflecting frequency selective surface, it can be assumed to be unity. Therefore,

$$1 = 4\left(\frac{a}{r}\right)^2\left(\frac{r}{\lambda}\right)^2 \times \ln\csc\left(\frac{\pi \cdot width}{2r}\right)\ln\csc\left(\frac{\pi \cdot gap}{2r}\right) \tag{8}$$

Putting $\csc(x) = \frac{1}{\sin(x)}$ in Eq. (8),

$$1 = 4\left(\frac{a}{r}\right)^2\left(\frac{r}{\lambda}\right)^2 \times \ln\left(\frac{1}{\sin\dfrac{\pi \cdot width}{2r}}\right)\ln\left(\frac{1}{\sin\dfrac{\pi \cdot gap}{2r}}\right) \tag{9}$$

It is obvious that the width of the unit cell is very much less than the periodicity, and the gap dimension is also very much less than the periodicity 'r'. This makes the angle of incidence very small. Therefore, $\sin(x) \approx x$ as

$$1 = 4\left(\frac{a}{r}\right)^2\left(\frac{r}{\lambda}\right)^2 \times \ln\left(\frac{2r}{\pi \cdot width}\right)\ln\left(\frac{2r}{\pi \cdot gap}\right) \tag{10}$$

The gap dimension is higher than the width for a given configuration: $(\frac{2r}{\pi \cdot width}) > (\frac{2r}{\pi \cdot gap})$. Therefore,

$$1 = 4\left(\frac{d}{\lambda}\right)^2 \times \ln\left(\frac{2p}{\pi \cdot width}\right) \tag{11}$$

To neglect the occurrence of grating lobes, the relationship between wavelength and periodicity is given by [37]

$$r(1 + \sin\theta) < \lambda \tag{12}$$

The above Equation (12) can be rewritten by fixing the value of 'r' by using a constant N which ranges between 0 and 1 as

$$r = N\lambda \tag{13}$$

By substituting Eq. (13) in Eq. (11),

$$1 = 4\left(\frac{a}{\lambda}\right)^2 \times \ln\left(\frac{2N\lambda}{\pi \cdot width}\right) \tag{14}$$

Therefore, Eq. (14) explains that if the design frequency is known, then the approximated width of the unit cell is a fraction of λ, and the value of reflection can be controlled.

To explain the wide bandwidth of the designed antenna, the mutual coupling effect between the elements of the metasurface layer is a critical point that has been diminished by tuning the optimal element size (a, b) and spacing gap (Dx, Dy). In this scenario, two different behaviors can be observed due to the capacitive coupling and surface wave coupling effects. Therefore, it will either react to cancel the current of the elements with each other or react to merge the two operating bands. This metasurface loading suppresses the mutual coupling effect (at designed frequencies, the currents induced from the conducting elements may negate the incident wave and prevent it from propagating through the set of elements). As a result, the operating bands are merged to give a widened band. The design was done by perfectly choosing the element size using the parametric analysis of Fig. 4. Accordingly, to broaden the bandwidth, the optimized 7 mm gap ($D_x = D_y = 7$ mm) was maintained between elements in the proposed metasurface layer.

A parametric study has been done to adjust the slot size for minimum reflection coefficient by varying a and b from 1 mm to 4 mm (at 4.6 GHz), and the results are shown in Fig. 4. As can be observed in the figure, the lowest reflection phase value depicted in the curve is for $a = 3$ mm and

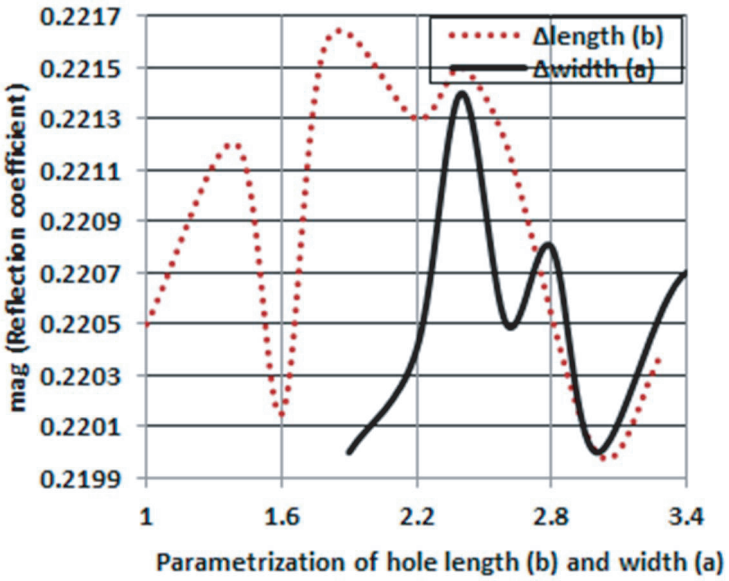

Figure 4. A parametric analysis results of metasurface reflection coefficient for minimum reflection.

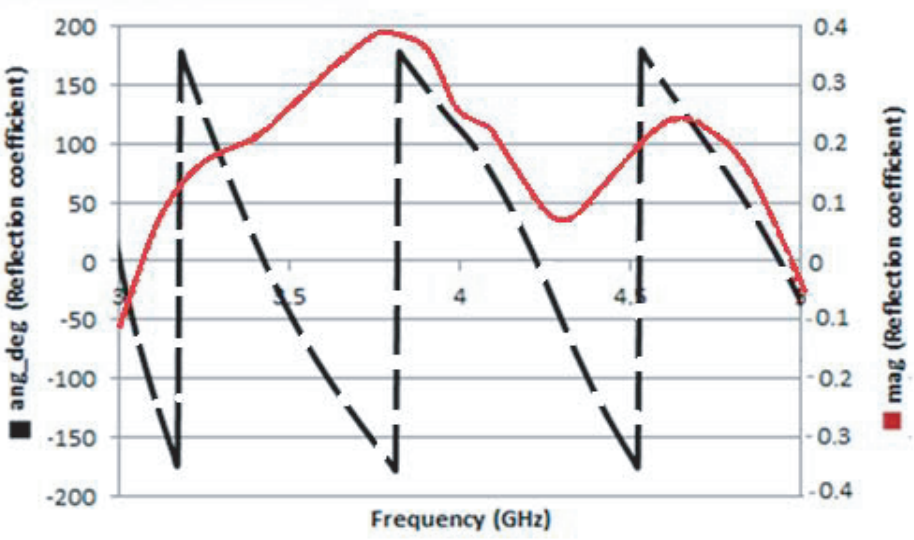

Figure 5. Reflection phase and magnitude of proposed embedded metasurface with Floquet port set-up for FEM Analysis.

$b = 3\,\text{mm}$. Hence, the minimum optimized reflection coefficient was 0.22. The simulated reflection phase (φ) of the designed embedded metasurface versus frequency is shown in Fig. 5. It is obvious that the phase is 150°, and the reflection magnitude (p) is 0.22.

2.2. Metasurface Design

To characterize the metasurface, it is imperative to extract its effective parameters using the parameter retrieval method [38] as in Eqs. (15), (16)

$$\varepsilon_{eff} = 1 + \frac{(2 * j)\,(1 - S_{11} - S_{21})}{(k_o * d)\,(1 + S_{11} + S_{21})} \tag{15}$$

$$\mu_{eff} = 1 + \frac{(2 * j)\,(1 + S_{11} - S_{21})}{(k_o * d)\,(1 - S_{11} + S_{21})} \tag{16}$$

The retrieved values of effective permeability (μ_{eff}) and effective permittivity (ε_{eff}) are shown in Fig. 6. In the presented results, it can be seen that they are approaching zero. Next, the refractive index (n) can be evaluated as $\sqrt{\mu_{eff} \cdot \varepsilon_{eff}}$. The near-zero-index band is possible as a result of the overlap of electric and magnetic resonances. At these regions, the transition from a negative-n region to a positive-n region is possible at the design frequency. The presented results conclude that there is a near-zero refractive index at the design frequency which will yield high directivity.

According to generalized Snell's law in Eq. (17) for an incident wave from a metasurface layer whose index of refraction = n_1 into a medium whose index of refraction n_2 [39]

$$n_2 \sin\theta_2 - n_1 \sin\theta_1 = k_0^{-1} \nabla\Phi \tag{17}$$

where $k_0^{-1}\nabla\Phi$ is the phase shift gradient along with the interface, θ_1 the incidence angle (crossing angle), and θ_2 the transmitted angle (emitted angle). This is equivalent to the electromagnetic wave that originates from the patch (source implanted inside a material block) and middle of the substrate at metasurface with near-zero refractive index (θ_1) emitting waves in a direction parallel to the normal (θ_2). This can increase the antenna directivity.

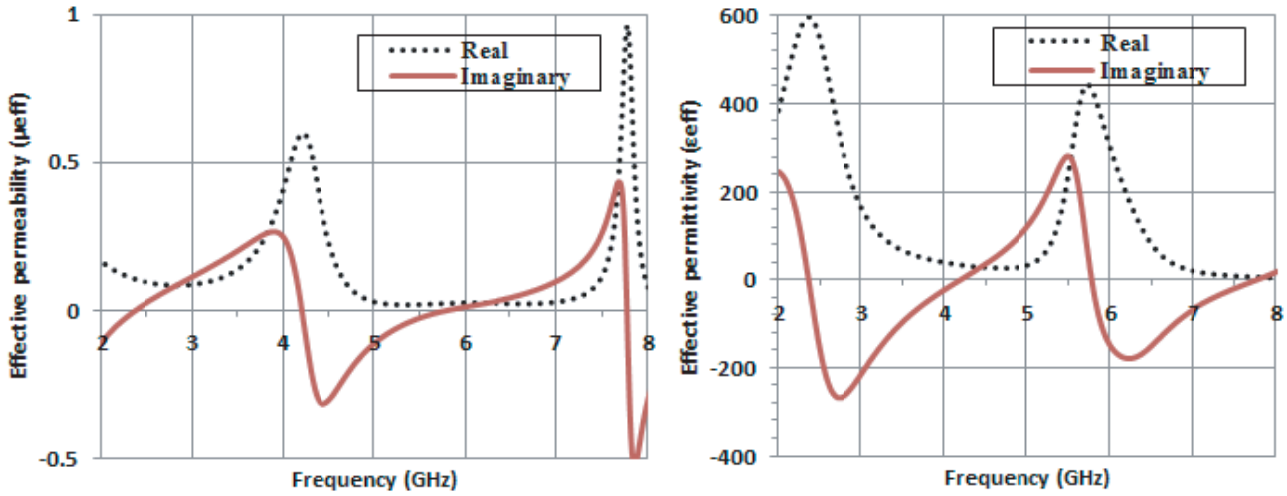

(a) (b)

Figure 6. (a) The calculated effective permeability and (b) the calculated effective permittivity of the embedded metasurface structure.

2.3. Metasurface Design

Transmission line modeling of the patch antenna has been used for evaluating the resonance frequency. The modeling of the patch as a lossy cavity is done concerning the cavity model, where electric walls at the top and bottom and magnetic walls at left and right surround the inner region. Therefore, modeling a microstrip patch antenna at resonance can be done as shown in Fig. 7(a). It is a parallel circuit of resistor (R), inductor (L), and capacitor (C) where R represents radiative and dissipative losses, and L, C represent the stored magnetic and electric energies. The values of R, L, C have been computed using schematic representation in commercial software Microwave Office (AWR) as $R = 75.784\,\Omega$, $C_1 = 1.42\,\text{pF}$, $L = 0.67\,\text{nH}$, and coupling capacitor $C_2 = 0.57\,\text{pF}$.

For the sake of validation, the transmission line model was used for the given cavity model representation of microstrip patch antenna, and a comparison between the computed reflection coefficients from schematic and from HFSS simulation is shown in Fig. 7(b) where a good agreement is evident. Also, the figure confirms the narrow band of the $-10\,\text{dB}$ reflection coefficient ($4.5\,\text{GHz}$–$4.7\,\text{GHz} \approx 4.3\%$).

The dielectric layer of $H/2$ height is sandwiched between the derived equivalent circuit model of the patch and the proposed equivalent schematic of the metasurface. The layer is represented by a lossy transmission line with characteristic impedance ($Z_{0\text{TL1}} = 235\,\Omega$) and a length equal to half of the substrate height at which embedded metasurface is placed as shown in Fig. 8.

The metasurface layer consists of square holes, and it acts as a reflector for the incoming electromagnetic waves at the resonant frequency. Thereby behaving as a band-stop filter [40], which can be represented as a series connection of L-C network whose impedance is given in Eq. (18)

$$Z_{square} = \frac{-\left(1+\rho_1 e^{-j\varphi}\right) Z_o^2}{2Z_o(|\rho_1|\, e^{-j\varphi})}\,[\Omega] \tag{18}$$

where $\rho_1 e^{-j\varphi}$ is the reflection coefficient of the metasurface structure, and Z_o is the free space impedance of $377\,\Omega$. The left-hand transmission line equivalent characteristic impedance is given by Eq. (19) assuming negligible loss,

$$Z_{(square)eq} = \omega L - \frac{1}{\omega C}\,[\Omega] \tag{19}$$

From Eqs. (18) and (19), the corresponding 'L_{eq}' and 'C_{eq}' are computed by obtaining the impedance of metasurface '$Z_{squarein}$' for the inner loop of the hole and '$Z_{squareout}$' for the outer loop of

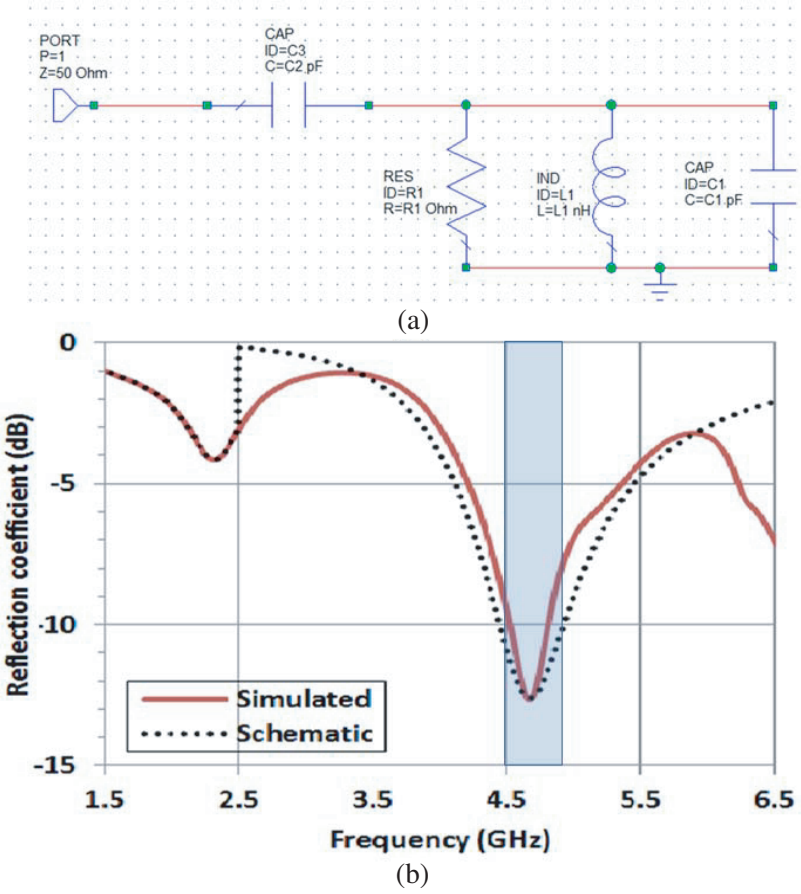

Figure 7. Microstrip patch antenna analysis. (a) Equivalent circuit schematic in AWR Microwave Office. (b) Comparison between simulated reflection coefficient values and proposed schematic model parameters.

the hole at two frequencies 'ω_1' and 'ω_2'

$$L_{eq} = \frac{Z_{squarein} + \dfrac{1}{\omega_1 C_{eq}}}{\omega_1} \text{ [H]} \tag{20}$$

$$C_{eq} = \frac{\omega_1^2 - \omega_2^2}{\omega_1 \omega_2^2 Z_{squarein} - \omega_2 \omega_1^2 Z_{squareout}} \text{ [F]} \tag{21}$$

The optimization of values in the AWR schematic was done by the curve fitting technique where the values of unknown parameters are tuned within a given range.

The height H between metasurface and patch antenna is maintained 0.8 mm. Hence, the proposed parameters have been optimized using AWR schematic as $C_6 = 37.51$ pF, $L_5 = 1.5$ nH, $C_4 = 0.68$ pF, $L_3 = 1.46$ nH, $C_5 = 1.64$ pF for the PRS. The value of loss for transmission line section between patch and PRS is 20.58, and the value of loss for transmission line section between PRS and ground plane is 21.91. The values of coupling capacitors and resistors C_3, C_8, and R_2 are 4.99 pF, 42.67 pF, and 235 Ω, respectively. The schematic simulated reflection coefficient using the embedded metasurface substrate analysis is plotted in Fig. 9. It has been found that the structure resonates at 2.0 GHz (FBW = 15%) and 4.6 GHz (FBW = 43%). The cause of two resonances is mainly the coupling of patch antenna with metasurface on top and bottom sides.

To validate the theoretical analysis, a comparison between the reflection coefficient obtained using AWR and the simulated results from HFSS is done and plotted in Fig. 9. It can be noticed that the

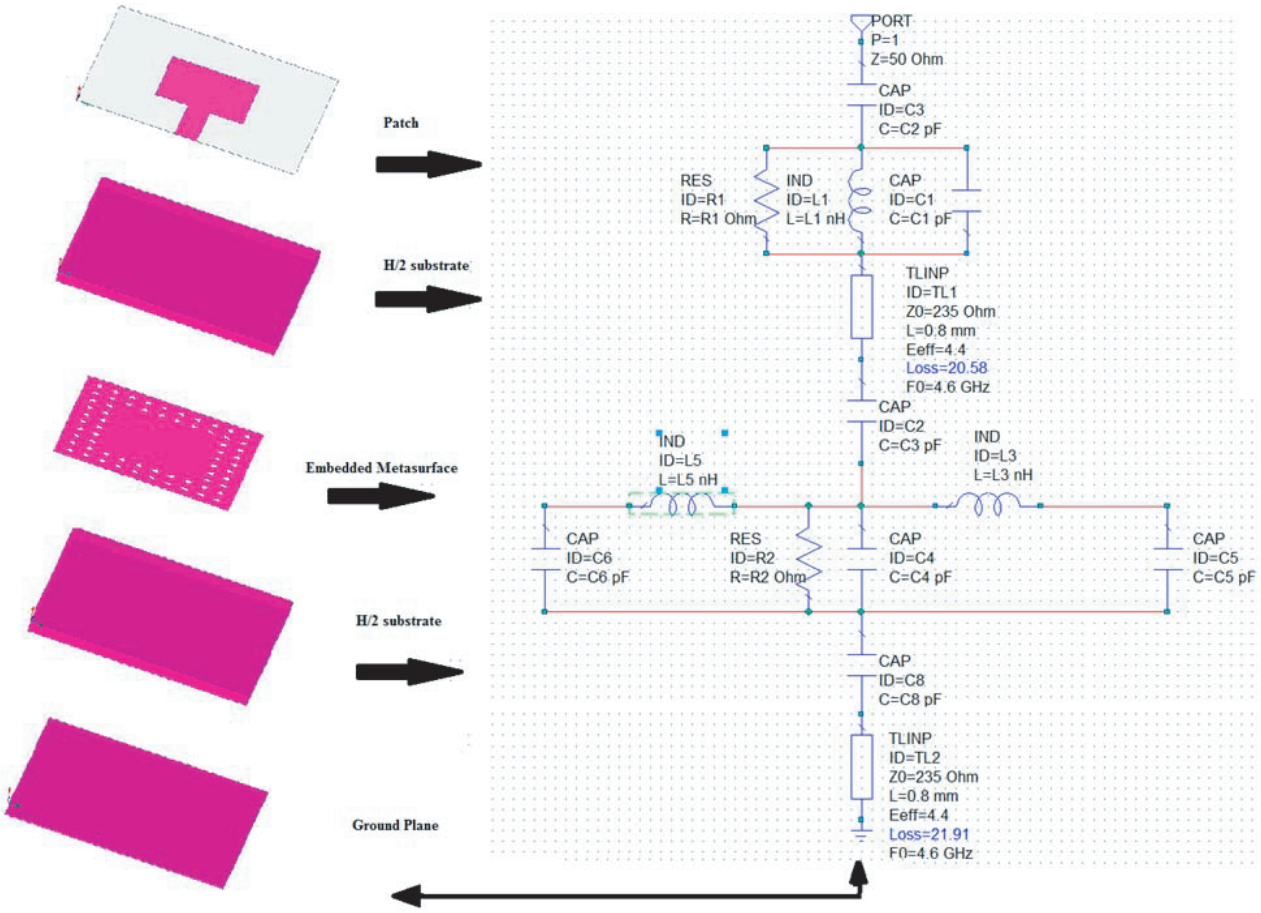

Figure 8. Composite Structure Analysis, equivalent circuit schematic in AWR Microwave Office.

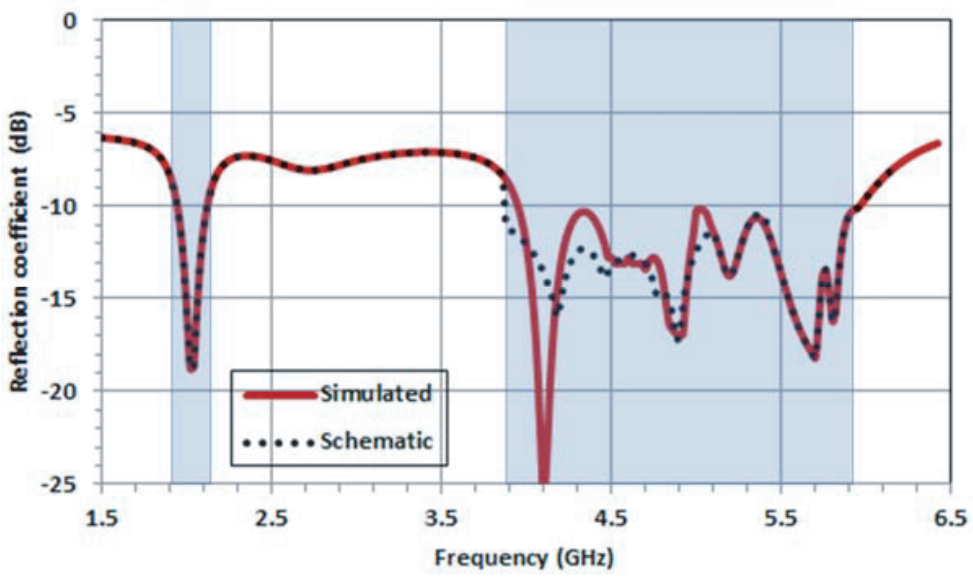

Figure 9. A comparison between simulated reflection coefficient values and proposed schematic model parameters.

proposed metasurface acts as a dual-band matching section between the antenna's substrate middle and ground plane leading to 56.5% miniaturization.

Finally, analysis of the antenna reflection coefficient by varying height of the metasurface below the patch is shown in Fig. 10. It is observed that the reflection coefficient is the lowest when metasurface is placed at $Hs/2$, i.e., in the middle of the antenna's substrate; the best performance of the antenna (lowest reflection coefficient) has been obtained.

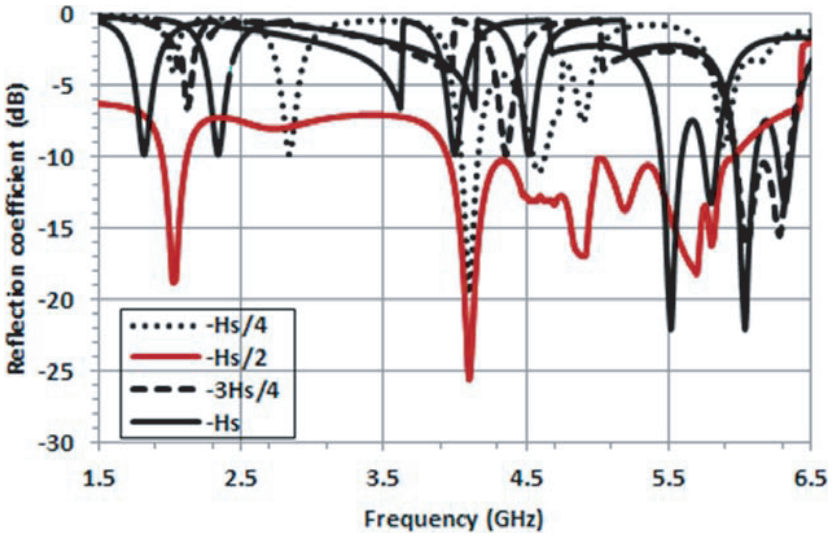

Figure 10. Comparison between simulated reflection coefficient (dB) for different heights of embedded metasurface below the patch.

3. ANTENNA RESULTS ANALYSIS AND DISCUSSION

3.1. Simulated Results

The simulated reflection coefficients of the unloaded and embedded metasurface loaded patch antenna are compared to each other in Fig. 11. The unloaded patch antenna is a narrow band antenna resonating at 4.6 GHz with a reflection coefficient = −12 dB. When the embedded metasurface is used, strong resonance is generated which enhances the matching. The −10 dB reflection coefficient bandwidth has increased more than ten times (3.9 GHz to 5.9 GHz, covering the original frequency (4.6 GHz)). Specifically, the reflection coefficient is −25 dB at 3.9 GHz and −18 dB at 5.7 GHz. Moreover, the antenna has another band centered at 2 GHz with −10 dB bandwidth from 1.9 GHz to 2.1 GHz.

The simulated gain in XZ and YZ planes for the conventional patch antenna and the metasurface embedded cases are plotted in Fig. 12(a) and Fig. 12(b), respectively. As shown in Fig. 12(a), the conventional patch antenna has gain = 3.2 dB and a front-to-back lobe ratio = 7. On the other hand, for the embedded metasurface-loaded antenna, the peak gain becomes 8.7 dB, and the Front-to-back lobe ratio is 187 (23 dB). This leads to a 171% improvement in gain and a 26 times improvement in front-to-back lobe ratio along with its physical protection.

Finally, the simulated current distribution at 4.6 GHz is shown in Fig. 13(a) for a single microstrip patch and Fig. 13(b) for the microstrip-loaded patch antenna. The confinement of the current is clear in the lens scenario using NZRIM. In other words, the exciting power flow is a strong enhancement in directivity from 5 dB of the conventional patch and exhibits a more intensely distributed current than the patch antenna itself. This further confirms the enhancement to 14 dB with loaded embedded metasurface. The same focusing phenomenon can be observed by emphasizing the current distribution at 2 GHz of the proposed embedded metasurface antenna as shown in Fig. 13(c). It can be shown that at 2 GHz the antenna's directionality is maintained, and an improvement is seen. This conclusion is further confirmed by plotting the simulated gain in XZ and YZ planes for the metasurface embedded antenna

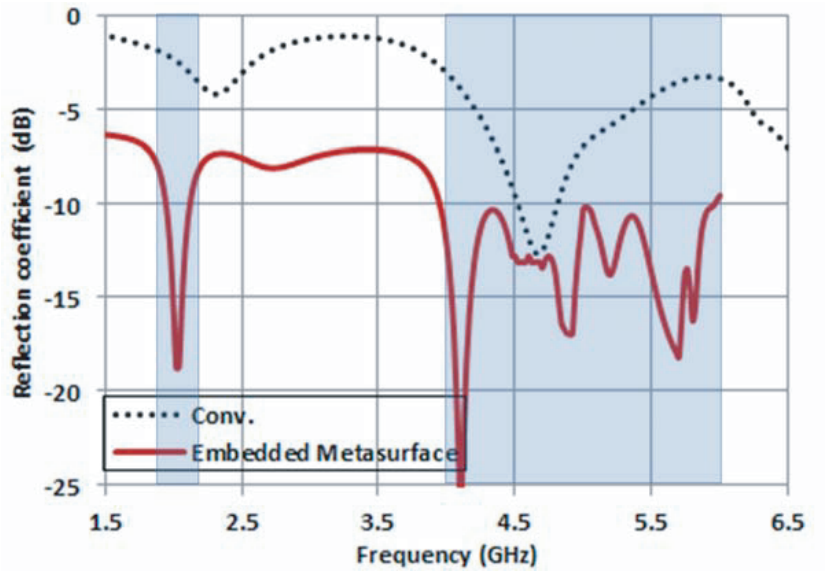

Figure 11. The simulated reflection coefficient for the proposed antenna (without and with using metasurface substrate).

in Fig. 12(c). It can be seen from the figure that peak gain becomes 7 dB, and the Front-to-back lobe ratio is 60 (15 dB). This leads to 118% improvement in gain and 9 times improvement in front-to-back lobe ratio along with its physical protection.

Finally, to confirm the antenna performance over the wideband width, the simulated antenna gain versus frequency is plotted in Fig. 14. The gain around the design frequency shows wideband nature.

It is worth commenting that the achieved directivity enhancement is valid for different oblique incident angles. To explain this point, the embedded metasurface can be assumed as a thin slab sandwiched by substrate medium as shown in Fig. 15. The boundary conditions are

$$1 + R = A + B \tag{22a}$$

$$Y_1(1 - R) = Y_2(A - B) \tag{22b}$$

$$C + D = T \tag{22c}$$

$$Y_2(C - D) = Y_1 T \tag{22d}$$

where $R =$ ratio of the reflected electric field to the incident electric field, $T =$ ratio of the transmitted electric field to the incident electric field; Y is the horizontal admittance for each medium; A, B, C, D are the counter-propagating waves inside the thin slab such that

$$A = Ce^{-jKt} \quad \text{and} \quad B = De^{-jKt} \tag{23}$$

Assuming that the thickness of the metasurface is such that $|kt| \ll 1$, in [41] it is proven that for oblique incidence kt is much smaller than the unit, and the constitutive parameters are much larger than the unit. It has also been proven in [42] that for a well-chosen metal thickness, angle and polarization-independent transmission is achievable assuming a square array of squared annular aperture patterned on a metal film embedded inside the antenna's substrate.

Finally, to elucidate the cross-polarization property of the proposed metasurface layer at 2 GHz, the polarization conversion ratio (PCR), which is defined as the ratio of the square of the cross-polarization reflection coefficient to the sum of the square of the co- and cross-polarization reflection coefficients, was calculated as in Eq. (24) [43–47]. For generating this calculation, a simulation of PRRS unit cell undergoes Floquet port analysis with master and slave boundaries for periodic structure analysis, shown earlier in Fig. 2. Assuming x-polarization incidence, cross- and co-polarized reflection coefficients are given by $R_{yx} = E_{yr}/E_{xi}$ and $R_{xx} = E_{xr}/E_{xi}$, where 'i' is for incident waves and 'r' for reflected waves. Similarly, for y-polarization incidence, cross- and co-polarization reflection coefficients are

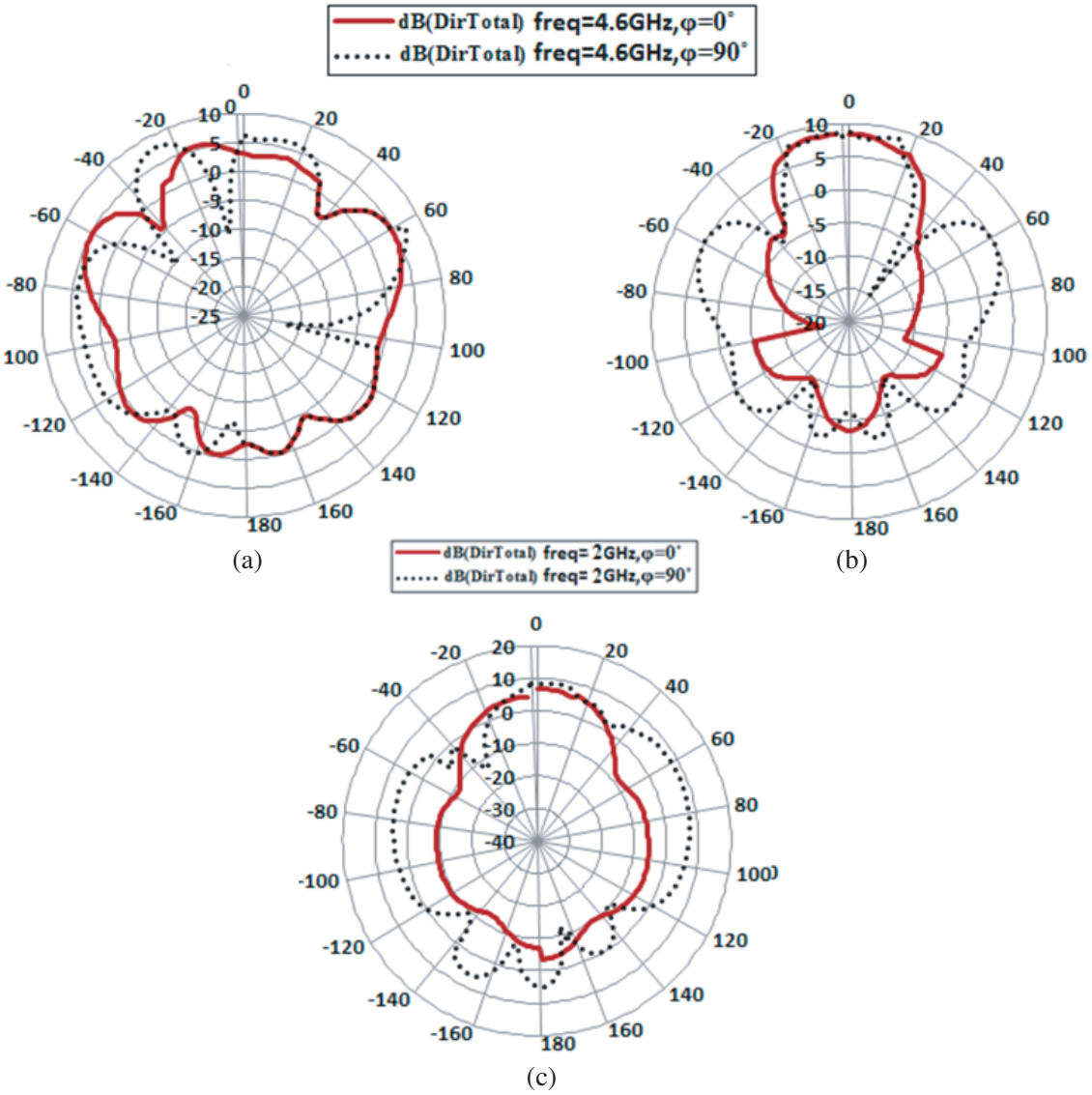

Figure 12. The simulated directive pattern for the (a) single patch antenna, (b) the proposed embedded metasurface antenna in XZ and YZ planes at 4.6 GHz, (c) the proposed embedded metasurface antenna in XZ and YZ planes at 2 GHz.

$R_{xy} = E_{xr}/E_{yi}$ and $R_{yy} = E_{yr}/E_{yi}$.

$$PCR = \frac{|R_{yx}|\,2}{|R_{yx}|2 + |R_{xx}|\,2} = \frac{|R_{xy}|\,2}{|R_{xy}|2 + |R_{yy}|\,2} \tag{24}$$

where

$r_{xy} = E_x^{Ref}/E_y^{Ref}$ $\rightarrow$ reflection ratio of y-to-x,

$r_{yy} = E_y^{Ref}/E_y^{Inc}$ $\rightarrow$ reflection ratio of y-to-y polarization conversions,

where E_y^{Inc} $\rightarrow$ electric field of the y-polarized incident EM wave

E_x^{Ref} $\rightarrow$ Electric fields of x-polarised reflected EM wave,

E_y^{Ref} $\rightarrow$ Electric fields of y-polarised reflected EM wave.

The PCR value of the proposed metasurface shows two resonances, with PCR measuring 98% for the first band (at 4.6 GHz) and PCR $\sim$ 60–90% for the second band (2 GHz). In these frequency ranges,

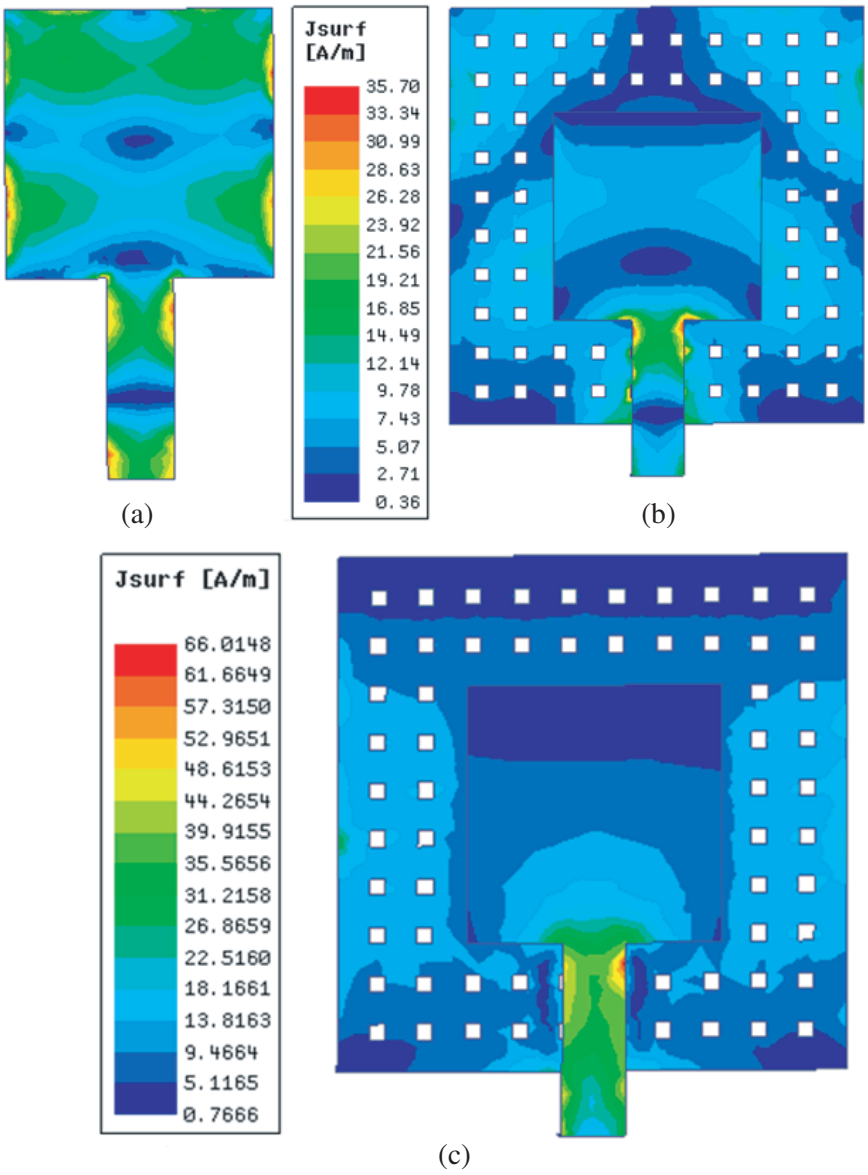

Figure 13. The simulated current distribution plot for (a) the patch antenna at 4.6 GHz, (b) the embedded metasurface antenna at 4.6 GHz, (c) the embedded metasurface antenna at 2 GHz.

a linearly polarized incident wave of known polarization state (x or y) is converted to the orthogonally polarized reflected wave (y or x), respectively (Fig. 16).

3.2. Measured Results

The fabricated prototype of the embedded metasurface antenna is shown in Fig. 17(a). The antenna is fabricated using the hot-pressing technique, where one FR4 substrate of thickness = 0.8 mm having patch on top is pressed against the second FR4 substrate with metasurface on top and copper ground at the bottom. The antenna performance was evaluated by checking its matching properties and EM radiation properties. The matching was tested by measuring the reflection coefficient (S_{11}) using Keysight RF Field fox Network Analyzer. On the other hand, the EM antenna radiation parameters were measured using SICO gain measurement setup shown in Fig. 17(b).

A comparison between simulated and fabricated structures is shown in Fig. 18. A very wide

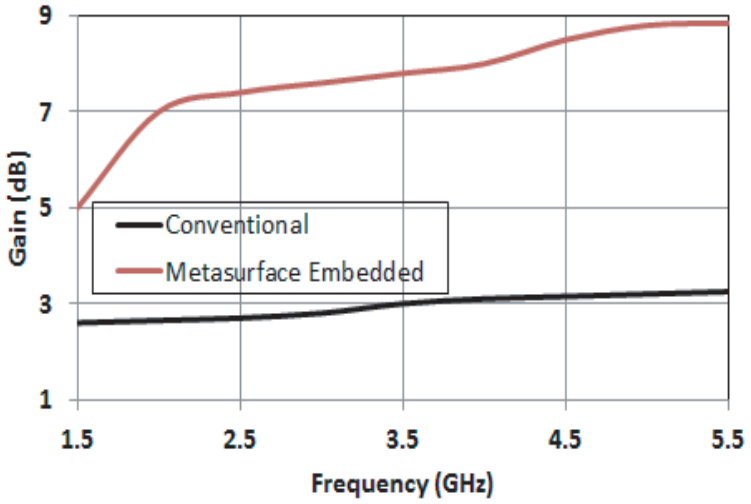

Figure 14. The simulated antenna gain vs frequency of the proposed embedded metasurface antenna versus conventional patch antenna at 2 GHz.

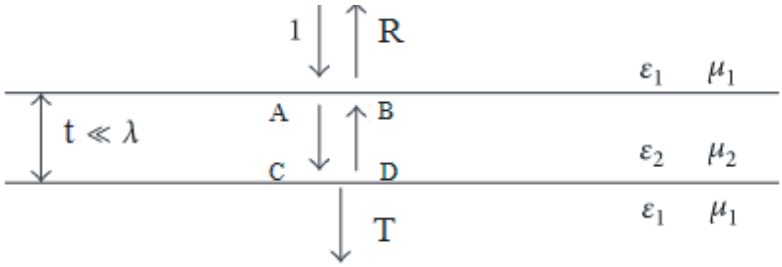

Figure 15. The thin slab embedded as metasurface inside antenna's substrate.

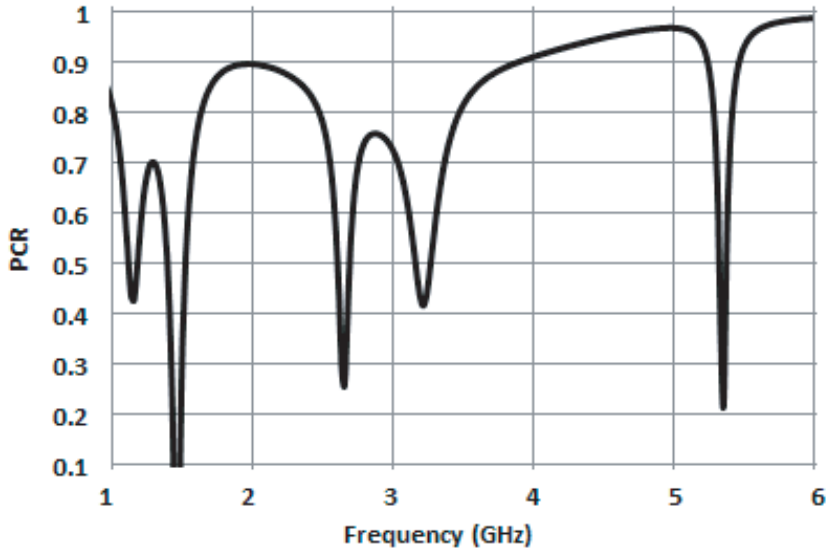

Figure 16. The simulated Polarization Conversion Ratio (PCR).

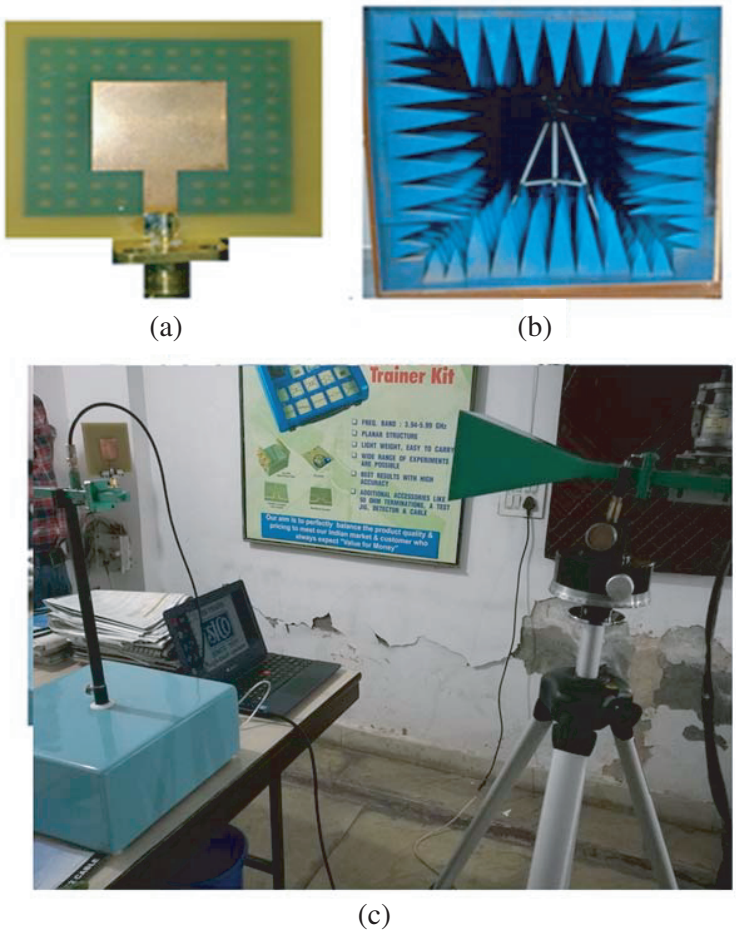

Figure 17. (a) The fabricated metasurface antenna prototype. (b), (c) The SICO Gain measurement set-up (b) the chamber setting, (c) the antenna gain measurement setting.

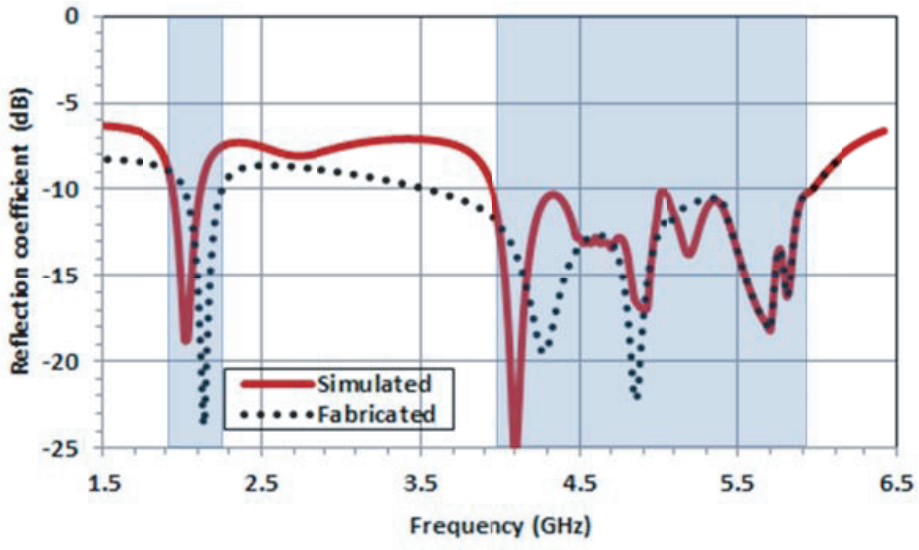

Figure 18. The simulated and measured reflection coefficient of the antenna.

bandwidth (associated with less than −10 dB) can be obtained when loading using the proposed FPC metasurface antenna. Good agreement between the simulated and measured curves with 5% error is obtained.

The comparison between the simulated and measured normalized radiation patterns in the E plane (XZ plane) and H plane (YZ) are plotted in Fig. 19(a) and Fig. 19(b), respectively. Very small discrepancies in the YZ plane at back lobes can be observed which can be claimed due to measurement limitations. The comparison confirms the effectiveness of the FPC antenna.

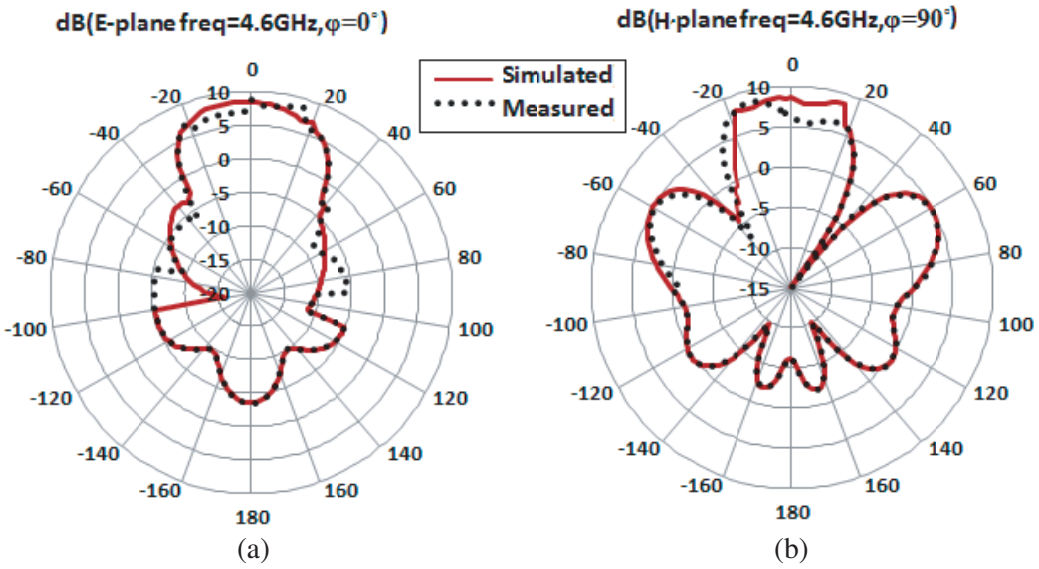

Figure 19. Comparison between simulated and measured directive Gain (dB) at 4.6 GHz of the metasurface antenna.

For antenna gain measurements, In the setup given by SICO in Fig. 17(c), the transmitted power is −40 dBm; received power is −73.04 dBm; transmitting antenna gain is 10 dB; and the distance between transmitting and receiving antennas is 2 meters. Using the *Friis* equation, the gain of receiving antenna is 8.7 dB, and the directivity is 14 dB. Therefore, a 6% error in peak gain of the fabricated antenna is obtained compared with simulated. The errors can be attributed to fabrication tolerances or testing environments.

3.3. Bandwidth Analysis with Varying Metasurface Parameters

In EM simulation, to emphasize the substrate losses effect on the computed FBW, the patch antennas with $\mathrm{Re}\{\varepsilon_r\} = 4.4$ were used for different values of tan δ_e. The simulated reflection coefficient and calculated fractional bandwidth results are plotted in Fig. 20(a) and Fig. 20(b) for the dielectric loss tangent variation from 0 and 0.1. It can be readily observed that when dielectric losses are increased, fractional bandwidth increases. Also, FBW increases if the loss tangent value is higher than 0.05. The basis of this finding illustrates that whenever losses are increased in antenna, the antenna becomes better matched at the cost of its radiation efficiency.

Finally, a comparison of the proposed antenna with existing state of art antenna structures using embedded metasurface is listed in Table 1. All the reference antennas have larger sizes. The FBW (%) of the proposed antennas is significantly more than the reference antennas; however, a few structures [21, 24] have higher directive gain. It is noticeable that the proposed antenna has the highest front-to-back lobe ratio.

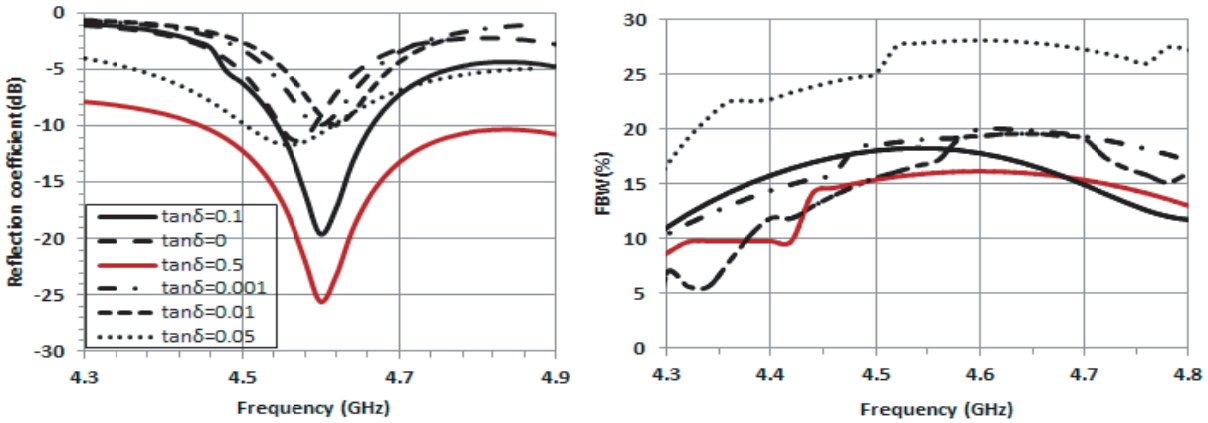

(a) (b)

Figure 20. When varying $\tan\delta m$ between 0 and 1. $\mathrm{Re}\{\varepsilon_r\} = 4.4$. (a) Reflection coefficient. (b) Fractional bandwidth.

Table 1. A comparison of the proposed work with reference antennas.

Reference	FBW (%)	Front/back ratio (dB)	Max. Directive Gain (dB)	Antenna Size
[20]	3.6	15	6.6	$2.75\lambda_0 \times 2.75\lambda_0 \times 0.56\lambda_0$
[21]	11.6	20	17.4	$2.83\lambda_0 \times 3.23\lambda_0 \times 0.49\lambda_0$
[22]	24	20	4	$3.87\lambda_0 \times 3.87\lambda_0 \times 1.77\lambda_0$
[23]	28	20	4.7	$2.4\lambda_0 \times 2.4\lambda_0 \times 1.4\lambda_0$
[24]	22.3	13	14.7	$2.77\lambda_0 \times 2.77\lambda_0 \times 0.69\lambda_0$
Our Work	43	23	14	$1.9\lambda_0 \times 1.9\lambda_0 \times 0.04\lambda_0$

4. CONCLUSION

A novel dual-band, directive, and miniaturized embedded metasurface antenna is designed and analyzed using a substrate with $\varepsilon_r = 4.4$. The novelty of this paper lies in choosing the position of the metasurface, i.e., in the middle of the antenna substrate. This position was left unexplored in literature. Using this technique, ten times increase in bandwidth and high miniaturization of the order of 56.5% is obtained as compared to the state of art. The antenna has dual-bands with 15% and 43% impedance bandwidths at 2 GHz and 4.6 GHz, respectively. With 171% improvement in gain and 26 times improvement in front-to-back lobe ratio, three times enhancement in directivity (with more than 3 dB directivity enhancement), this antenna shows maximum enhancements to the best of authors' knowledge making it an ideal candidate for the use in mobile communications, relevant radar systems, and imaging at microwave frequencies.

REFERENCES

1. Wong, K. L., *Compact and Broadband Microstrip Antennas*, Wiley, New York, NY, USA, 2002.
2. Lo, T. K., Y. Hwang, E. K. W. Lam, and B. Lee, "Miniature aperture-coupled microstrip antenna of very high permittivity," *Electron. Lett.*, Vol. 33, 9–10, 1997.
3. Lee, B. and F. J. Harackiewicz, "Miniature microstrip antenna with a partially filled high-permittivity substrate," *IEEE Trans. Antennas Propagat.*, Vol. 50, No. 8, 1160–1162, 2002.

4. Waterhouse, R., "Small microstrip patch antenna," *Electron. Lett.*, Vol. 31, No. 8, 604–605, 1995.
5. Wong, K. L. and Y. F. Lin, " Small broadband rectangular microstrip patch antenna with chip-resistor loading," *Electron. Lett.*, Vol. 33, No. 19, 1593–1594, 1997.
6. Ferrari, P., N. Corrao, and D. Rauly, "Miniaturized circular patch antenna with capacitors loading," *SBMO/IEEE MTT-S International Microwave and Optoelectronics Conference*, 86–89, Brazil, 2007.
7. Wong, K. L., C. L. Tang, and H. T. Chen, "A compact meandered circular microstrip antenna with a shorting pin," *Microwave Opt. Technol. Lett.*, Vol. 15, 147–149, 1997.
8. Nasimuddin, X. Q. and Z. N. Chen, "A compact circularly polarized slotted patch antenna for GNSS applications," *IEEE Trans. Antennas Propagat.*, Vol. 62, No. 12, 6506–6509, 2014.
9. Dong, Y. D., H. Toyao, and T. Itoh, "Compact circularly-polarized patch antenna loaded with metamaterial structures," *IEEE Trans. Antennas Propagat.*, Vol. 59, 4329–4333, 2011.
10. Kumar, G. and K. Gupta, "Nonradiating edges and four edges gap-coupled multiple resonator broad-band microstrip antennas," *IEEE Antennas Propag. Mag.*, 127–135, 2015.
11. Yang, M., Z. N. Chen, P. Y. Lau, X. Qing, and X. Yinl, "Miniaturized patch antenna with grounded strips," *IEEE Trans. Antennas Propagat.*, Vol. 63, No. 2, 2015.
12. Pozar, D. M., "Microstrip antennas," *Proceedings of the IEEE*, Vol. 80, No. 1, 79–91, 1992.
13. Long, S. and M. Walton, "A dual-frequency stacked circular-disc antenna," *IEEE Trans. Antennas Propagat.*, Vol. 27, No. 2, 1979.
14. Sullivan, P. and D. Schaubert, "Analysis of an aperture coupled microstrip antenna," *IEEE Trans. Antennas Propagat.*, Vol. 34, No. 8, 1986.
15. Maci, S., G. Biffi Gentili, P. Piazzesi, and C. Salvador, "Dual-band slot-loaded patch antenna," *IEE Proceedings — Microwaves, Antennas and Propagation*, Vol. 142, No. 3, 225–232, 1995.
16. Mohamad, S., R. Cahill, and V. Fusco, "Performance of Archimedean spiral antenna backed by FSS reflector," *Electron. Lett.*, Vol. 51, No. 1, 14–16, 2014.
17. Gonzalo, R., P. De Maagt, and M. Sorolla, "Enhanced patch-antenna performance by suppressing surface waves using photonic-bandgap substrates," *IEEE Trans. Microw. Theory Tech.*, Vol. 47, No. 11, 2131–2138, 1999.
18. Trentini, G. V., "Partially reflecting sheet arrays," *RE Trans. Antennas Propag.*, Vol. 4, No. 4, 666–671, 1956.
19. Holloway, C. L., E. F. Kuester, J. A. Gordon, J. O'Hara, J. Booth, and D. R. Smith, "An overview of the theory and applications of metasurfaces: The two-dimensional equivalents of metamaterials," *IEEE Antennas Propag. Mag.*, Vol. 54, No. 2, 10–35, 2012.
20. Yan, S., P. J. Soh, and G. A. E. Vandenbosch, "Compact all-textile dual-band antenna loaded with metamaterial inspired structure," *IEEE Antennas and Wireless Propagation Letters*, Vol. 14, 1486–1489, 2014.
21. Sharma, S., M. Abdalla, and Z. Hu, "Miniaturization of an electrically small metamaterial inspired antenna using additional conducting layer," *IET Microw. Antennas Propag.*, Vol. 12, No. 8, 1444–1449, 2018.
22. Yan, S., P. J. Soh, and G. A. E. Vandenbosch, "Low-profile dual-band textile antenna with artificial magnetic conductor plane," *IEEE Trans. Antennas Propagat.*, Vol. 62, No. 12, 6487–6490, 2014.
23. Yan, S., P. J. Soh, and G. A. E. Vandenbosch, "Wearable dual-band magneto-electric dipole antenna for WBAN/WLAN applications," *IEEE Trans. Antennas Propagat.*, Vol. 63, No. 9, 4165–4169, 2015.
24. Lubkowski, G., C. Damm, B. Bandlow, R. Schuhmann, M. Schßler, and T. Weiland, "Metamaterial loaded waveguides for miniaturized filter applications," *Frequenz*, Vol. 62, 3–4, 2018.
25. Jia, Y., Y. Liu, W. Zhang, J. Wang, S. Gong, and G. Liao, "High-gain Fabry-Pérot antennas with wideband low monostatic RCS using phase gradient metasurface," *IEEE Access*, Vol. 7, 4816–4824, 2019.
26. Jiang, H., Z. Xue, M. Leng, W. Li, and W. Ren, "Wideband partially reflecting surface antenna with broadband RCS reduction," *IET Microw., Antennas Propag.*, Vol. 12, No. 6, 94194, 2018.

27. Mu, J., H. Wang, H. Wang, and Y. Huang, "Low-RCS and gain enhancement design of a novel partially reflecting and absorbing surface antenna," *IEEE Antennas and Wireless Propagation Letters*, Vol. 16, 1903–1906, 2017.
28. Zheng, Y., J. Gao, Y. Zhou, X. Cao, H. Yang, S. Li, and T. Li, "Wideband gain enhancement and RCS reduction of Fabry-Pérot resonator antenna with chessboard arranged metamaterial superstrate," *IEEE Trans. Antennas Propagat.*, Vol. 66, No. 2, 590599, Feb. 2018.
29. Singh, A. K., M. P. Abegaonkar, and S. K. Koul, "High-gain and high-aperture-efficiency cavity resonator antenna using metamaterial superstrate," *IEEE Antennas and Wireless Propagation Letters*, Vol. 16, 2388–2391, 2017.

30. Dawar, P. and M. A. Abdalla, "Near-zero-refractive-index metasurface antenna with bandwidth, directivity and front-to-back radiation ratio enhancement," *Journal of Electromagnetic Waves and Applications*, Vol. 35, No. 14, 1863–1881, 2021.
31. Deng, F. and J. Qi, "Shrinking profile of Fabry-Perot cavity antennas with stratified metasurfaces: Accurate equivalent circuit design and broadband high-gain performance," *IEEE Antennas and Wireless Propagation Letters*, Vol. 19, No. 1, 208–212, 2020.
32. Pham, D. A., E. Park, H. L. Lee, and S. Lim, "High gain and wideband metasurfaced magneto-electric antenna for WiGig applications," *IEEE Trans. Antennas Propagat.*, Vol. 69, No. 2, 1140–1145, 2021.
33. Marcuvitz, N., *Waveguide Handbook*, Vol. 21, Peter Peregrinus Ltd., New York, 1986.
34. Langley, R. J. and E. A. Parker, "Equivalent circuit model for arrays of square loops," *Electron. Lett.*, Vol. 18, No. 7, 294–296, 1982.
35. Lee, C. K. and R. J. Langley, "Equivalent-circuit models for frequency selective surfaces at oblique angles of incidence," *IEE Proceedings — H, Microwaves Optics and Antennas*, Vol. 132, 395–399, 1985.
36. Saraswat, R. K. and M. Kumar, "A metamaterial loaded hybrid fractal multiband antenna for wireless applications with frequency band reconfigurability characteristics," *Frequenz*, Vol. 74, No. 11–12, Sept. 2020.
37. Reed, J. A., "Frequency selective surfaces with multiple periodic elements," Ph.D. Thesis, University of Texas Dallas, USA, 1997.
38. Liu, A., S. Lei, X. Shi, and L. Li, "Study of antenna superstrates using metamaterials for directivity enhancement based on Fabry-Perot resonant cavity," *International Journal of Antennas and Propagation*, Vol. 2013, 1–10, 2013.
39. Peng, X., G. Wang, H. Li, and X. Gao, "A novel methodology for gain enhancement of the Fabry-Pérot antenna," *IEEE Access*, Vol. 7, 176170–176176, 2019.
40. Uddin, M. J., M. H. Ullah, T. A. Latef, W. N. Mahadi, and M. T. Islam, "Making meta better: The synthesis of new-shaped periodic artificial structures suitable for metamaterial behavior characterization," *IEEE Microw. Mag.*, Vol. 8, No. 17, 52–58, 2016.
41. Karlsson, A., "Approximate boundary conditions for thin structures," *IEEE Trans. Antennas Propagat.*, Vol. 57, No. 1, 144–148, 2009.
42. Van Labeke, D., D. Gérard, B. Guizal, F. I. Baida, and L. Li, "An angle-independent frequency selective surface in the optical range," *Optics Express*, Vol. 14, No. 25, 11945–11951, 2006.
43. Liu, Y., S. Xia, H. Shi, A. Zhang, and Z. Xu, "Dual-band and high-efficiency polarization converter based on metasurfaces at microwave frequencies," *Appl. Phys. B*, Vol. 122, 178, 2016.
44. Mustafa, M. E., F. A. Tahir, and M. Amin, "Broadband waveplate operation by orthotropic metasurface refector," *J. Appl. Phys.*, Vol. 126, 2019.
45. Li, J., et al., "Dual-band transmissive cross-polarization converter with extremely high polarization conversion ratio using transmitarray," *Materials*, Vol. 12, No. 1827, 2019.
46. Cao, H., et al., "Dual-band polarization conversion based on non-twisted Q-shaped metasurface," *Opt. Comm.*, Vol. 370, 311–318, 2016.
47. Khan, M. I., Q. Fraz, and F. A. Tahir, "Ultra-wideband cross polarization conversion metasurface insensitive to incidence angle," *J. Appl. Phys.*, Vol. 121, 045103, 2017.